

AeCoM: An Aerial Continuum Manipulator With IMU-Based Kinematic Modeling and Tendon-Slacking Prevention

Rui Peng[✉], Zehao Wang, and Peng Lu[✉]

Abstract—This article presents a novel aerial manipulator (AM) system called the aerial continuum manipulator (AeCoM). The system is comprised of a quadrotor and a tendon-driven continuum robotic manipulator. Compared to current AMs, the AeCoM has the advantages of being lightweight and having high dexterity. The continuum manipulator has two contributions: 1) the development of an IMU-based kinematic model to obtain the precise end-effector pose under external loading and 2) the design of a robust closed-loop kinematic controller that implements fast shape-deformation control and prevents tendon slacking by providing feedback of the configuration space and torque applied on tendons. The article provides a detailed mechanical design of the system and extensive experiments were conducted to validate the system’s performance.

Index Terms—Aerial system, design, modeling and control, tendon-driven continuum robot.

I. INTRODUCTION

A. Aerial Manipulators

THE USE of aerial manipulators (AMs) has been explored in various studies, such as [1], [2], [3], [4], [5], and [6]. There are two predominant types of UAV platforms used for AM which are unmanned helicopters and multirotor UAVs. Unmanned helicopters are difficult to operate precisely due to their complex mechanisms and complicated aerodynamic characteristics [7]. On the other hand, multirotor UAVs, such as quadrotor, hexa-rotor, and octo-rotor, are more popular for AM applications due to their mechanical simplicity, easy-to-deploy flight controller design, low vibration, low cost, and flying dexterity in both indoor and outdoor environments [8], [9].

There are two main categories of manipulation mechanisms used in AM systems: 1) grippers and 2) robotic manipulators. Grippers are typically installed under the UAV fuselage and located near the center-of-mass (CoM) of the overall system. Grippers have little impact on the UAV dynamics [10]. Robotic

Manuscript received 15 November 2022; accepted 9 March 2023. This work was supported in part by the General Research Fund under Grant 17204222, and in part by the Seed Funding for Strategic Interdisciplinary Research Scheme and Platform Technology Fund. This article was recommended by Associate Editor X. Wu. (*Corresponding author: Peng Lu*)

The authors are with the Adaptive Robotic Controls Lab, Department of Mechanical Engineering, The University of Hong Kong, Hong Kong, China (e-mail: pengrui-rio@connect.hku.hk; lupeng@hku.hk).

This article has supplementary material provided by the authors and color versions of one or more figures available at <https://doi.org/10.1109/TSMC.2023.3257166>.

Digital Object Identifier 10.1109/TSMC.2023.3257166

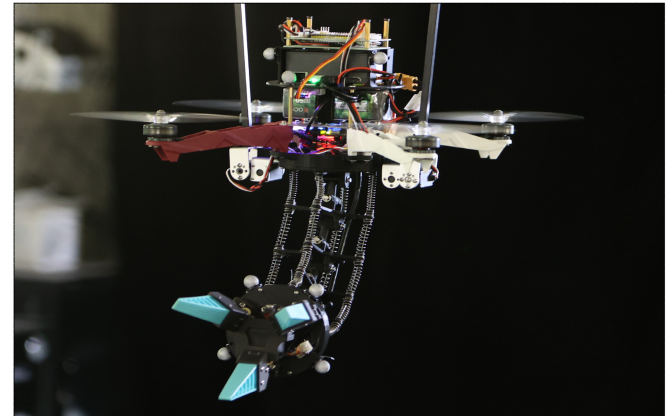


Fig. 1. Authors develop the original prototype of an AeCoM, which is conducting aerial grasping operations.

manipulators have multiple degrees of freedom (DOFs) which contribute to an extensive workspace, enabling numerous functionalities, and enhancing mission adaptability [11].

Although AM systems have numerous advantages and potential, there are some critical issues that need to be addressed. These issues are explored as follows.

- 1) Aerial platforms, such as helicopters or octo-rotor UAVs, are limited in flying in unstructured and restricted spaces due to their relatively large airframes and propellers. Additionally, the large manipulator part adds significant weight to the overall system, making it much heavier.
- 2) Lightweight UAVs can only carry grippers or robotic manipulators with few DOFs. The functionality of the manipulators is restricted by the UAV platform, limiting potential aerial applications [12].
- 3) Specific manipulators are designed for special manipulation tasks but may lack flexibility and extensibility.

To overcome the aforementioned issues, a novel type of robotic manipulator called continuum robots is explored due to their increased flexibility and low weight, [13], [14]. The concept of an aerial continuum manipulator (AeCoM) based on a simulation model is theoretically proposed by Samadikhoshkho et al. [15]. However, in this article, the authors design and manufacture an actual AeCoM composed of a lightweight quadrotor platform and a continuum robotic manipulator as shown in Fig. 1. The weight of the UAV

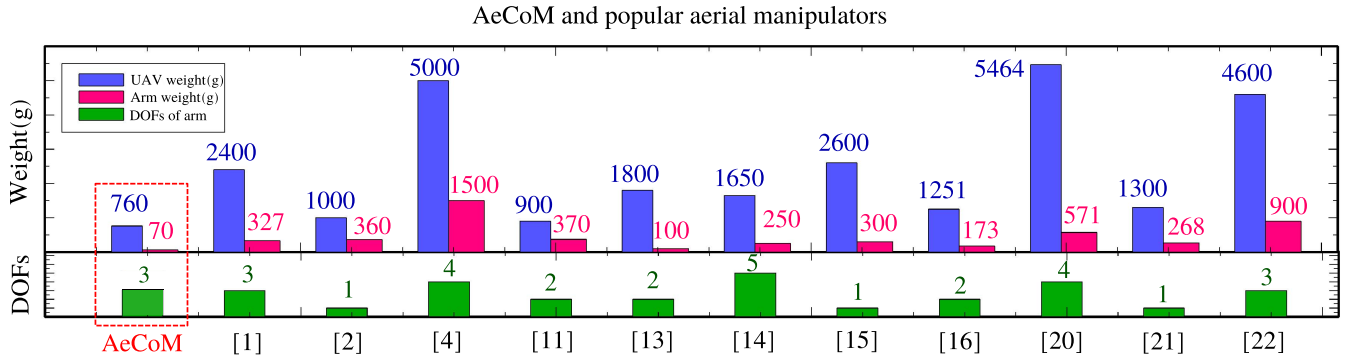


Fig. 2. Mechanism properties comparison with current AMs. A histogram of UAV weight, arm weight, and DOFs of the arm for comparing the AeCoM and current AMs. [1], [2], ..., [22] are published studies of AMs in the survey [1], [12].

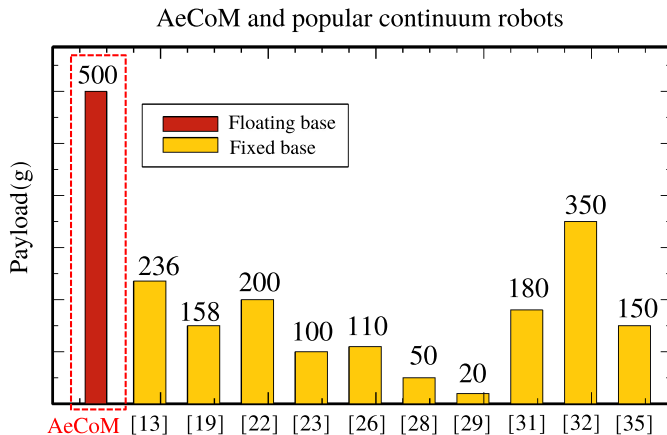


Fig. 3. Mechanism properties comparison with current continuum robotic manipulators. A histogram of the base property and payload limit for comparing the AeCoM and current continuum robots. [13], [19], ..., [35] are published continuum robots in the survey [14].

platform is 760 g, and its size is 320 × 320 mm. The manipulator part, which weighs only 60 g, is tendon driven and has one section with five segments, providing the AeCoM with aerial manipulation capability.

To compare the AeCoM with conventional AMs, the weight, and DOFs of the manipulator are considered as the two main factors. Fig. 2 presents a comparison chart between AeCoM and conventional AMs based on UAV weight, robotic arm weight, and DOFs of the arm. It is evident that the AeCoM has the lowest weight for both the UAV platform and the robotic arm, and it has three DOFs. While there are other AeCoMs in recent literature, such as [15], [16], [17], and [18], only present simulation models without designing an actual AeCoM. Chien et al. [16] has an external actuation system separated from the aerial system, while [17] only designs the continuum manipulator part without the aerial platform. Additionally, none of these studies have conducted actual flight experiments. In contrast, the AeCoM has a complete self-independent mechanical and hardware system, which strongly supports experimental validation and comparison.

To compare the AeCoM with current continuum robots, the payload capacity is considered as the key factor, as it determines the maximum limit of loading. Fig. 3 compares

the payload capacity of the AeCoM's continuum manipulator with current continuum robots, showing that the AeCoM has a floating base with much better mobility, and its experimental payload capacity is the highest at 500 g. In contrast, most continuum robots have fixed bases due to the difficulty in mechanically reducing the weight and volume of their actuation part. However, due to the use of lightweight actuation motors and compacted mechanical design in the AeCoM, a mobile base (i.e., floating) for the continuum manipulator is possible.

B. Continuum Robot

The end-effector (EE) pose, which is derived from the manipulator kinematics model, has a direct impact on the performance of aerial manipulation tasks. However, the conventional tendon-length-based kinematics model [13], commonly used in continuum robots, fails to compute precise shape deformation under external loading due to nonlinear and uneven force distribution. To address this issue, several techniques have been investigated, including data-driven techniques [19], [20], sensor-feedback methods [21], [22], and mathematical models [23], [24]. In this study, IMU sensors are employed to build a robust continuum kinematics model, considering uncertainties caused by variable loading.

Generally, continuum robots [25], [26], [27] critically suffer tendon slacking and commonly have slow motion. Also, they are vulnerable to external disturbance, such as unknown loading. From the perspective of control, model-based controllers are used widely for the control of soft or continuum robots. Further on, studies [28], [29], [30], [31], [32], [33], [34] have explored the importance of sensors for compensating model uncertainties in controller design to reduce tracking error. However, these methods are applicable on static states and are not able to cope with fast motion. Considering the sensor-based configuration space and internal actuation forces, the authors design a robust closed-loop kinematic controller for the AeCoM's manipulator system to implement fast shape-deformation control, in order to tackle variable loading and tendon slacking. Experiments validate that the manipulator's EE achieves extremely low tracking errors during the consecutive attitude tracking motion, without tendon slacking.

C. Contributions

To prove the feasibility of the AeCoM, the authors conduct detailed experimental validation and comparison. Potential applications, such as agricultural harvesting, delivery service, industrial inspection, etc, will be explored in the future. The main contributions of this article can be summarized as follows.

- 1) A novel AeCoM is proposed with a lightweight and comprehensive mechanism design. The system has the advantages of exceptional locomotion dexterity and payload capacity over conventional aerial rigid manipulators.
- 2) An IMU-based kinematics modeling method for the continuum manipulator is proposed to obtain precise EE poses under external loading. Experiments of aerial spatial motion and object grasping are conducted to prove the distinct accuracy.
- 3) By employing IMU and torque sensors, a robust closed-loop kinematic manipulator control method is derived to implement fast shape-deformation control and prevent tendon slacking during aggressive spatial motion.

II. DESIGN

In this section, an overview of the system architecture is illustrated in detail, including the hardware design and the mechanism structure.

To incorporate a continuum robotic system into an aerial platform, the entire weight, payload capacity, and control accuracy or dexterity should be considered [24]. Instead of pneumatic driving which lacks control accuracy, the authors deploy a tendon-driven system to control the continuum manipulator. To achieve a larger workspace, the proposed prototype consists of five consecutive segments to extend its spatial range, as shown in Fig. 4. Each segment is composed of two cross disks, which are connected by a mechanical gimbal with four evenly distributing springs. The spatial motion is actuated by four tendons that are driven by four actuation motors with torque feedback. Of note, the key factor of the production of the manipulator is the usage of the specific motor whose weight is only 20 g. In addition, each motor could provide a maximum torque of 4.5 kg · cm, and its volume is 8 cm³. The exceptional properties of the motor facilitate the optimization of the system's structural layout, especially, the highly compacted actuation part. The ratio between the volume of the actuation part and the volume of the whole manipulator, decreases down to only 7.69%, also as shown in Fig. 4 (c) and (i).

The hardware architecture is divided into two independent subsystems: 1) a UAV platform and 2) a continuum robotic system. The hierarchical hardware design establishes the solid basis of the AeCoM. A high-performance onboard PC (DJI Manifold-v2) is responsible for receiving and processing sensing information, and generating unified motion commands. The UAV platform is a quadrotor with a size of 320 × 320 mm. The continuum robotic system involves a microcontroller board (STM32) as the core, torque sensors, IMUs, and four continuum-actuation motors. The latter two systems

directly connect to the onboard PC via serial ports, which form stable communication channels. Also, the system workflow, including signals communication between the three parts and key onboard tasks is shown in Fig. 5.

III. MODELING

This section presents the forward and inverse kinematics models of the AeCoM. To describe the configuration of the system, the authors introduce the world frame \mathcal{W} , the UAV body frame \mathcal{V} , the base frame of the manipulator \mathcal{B} , and the EE frame \mathcal{E} , as shown in Fig. 6. The generalized coordinates for the UAV platform, including UAV position $\mathbf{p}_u = [x_u \ y_u \ z_u]^T$ and attitude $\boldsymbol{\eta}_u = [\psi_u \ \theta_u \ \phi_u]^T$, with respect to the world frame, are defined. As for the continuum manipulator part, $\boldsymbol{\lambda}_{cm} = [\theta_{cm} \ \phi_{cm}]^T$ (subscript cm denotes the continuum manipulator) denoting the configuration space with respect to the base frame \mathcal{B} , is defined. θ_{cm} is the bending plane angle and ϕ_{cm} is the direction plane angle. Also, l_{cm} is the arc length, and r_{cm} is the radius of the continuum body. The number of segments is denoted as n_{cm} . The tendon actuation space $\mathbf{L}_{cm} = [l_1 \ l_2 \ l_3 \ l_4]^T$ denotes the tendon lengths of the continuum manipulator.

A. System Kinematics Model

The system kinematics model is established to describe spatial motion relationships between key coordinate frames ($\mathcal{W}, \mathcal{V}, \mathcal{B}, \mathcal{E}$). With the model, it is convenient to compute all the frames' poses with respect to the world frame. However, what authors are most concerned about is obtaining the accurate pose of the EE, which is crucial to versatile manipulation tasks. To achieve this, a fundamental kinematics chain is built for the system

$${}^{\mathcal{W}}\mathbf{P}_{ee} = \mathbf{P}_{\mathcal{W}} \cdot \mathbf{T}_{\mathcal{V}}^{\mathcal{W}} \cdot \mathbf{T}_{\mathcal{B}}^{\mathcal{V}} \cdot \mathbf{T}_{\mathcal{E}}^{\mathcal{B}} \quad (1)$$

where ${}^{\mathcal{W}}\mathbf{P}_{ee}$ denotes the pose of the EE in the world frame by the left superscript \mathcal{W} . $\mathbf{P}_{\mathcal{W}}$ numerically represents the world frame \mathcal{W} . $\mathbf{T}_{\mathcal{V}}^{\mathcal{W}}$ is a homogeneous matrix that describes the transformation from \mathcal{W} to \mathcal{V} , and the matrix can be obtained from external devices, such as VICON [35], VIO [36], etc. Similarly, $\mathbf{T}_{\mathcal{B}}^{\mathcal{V}}$ decided by the mechanical design from the CAD drawing, describes the transformation from \mathcal{V} to \mathcal{B} . $\mathbf{T}_{\mathcal{E}}^{\mathcal{B}}$ needs an applicable continuum kinematic model. $\mathbf{T}_{\mathcal{V}}^{\mathcal{W}}$, $\mathbf{T}_{\mathcal{B}}^{\mathcal{V}}$, and $\mathbf{T}_{\mathcal{E}}^{\mathcal{B}}$ are given by

$$\mathbf{T}_{\mathcal{V}}^{\mathcal{W}} = \begin{bmatrix} \mathbf{R}_{\mathcal{V}}^{\mathcal{W}} & \mathbf{t}_{\mathcal{V}}^{\mathcal{W}} \\ 0 & 1 \end{bmatrix}, \quad \mathbf{T}_{\mathcal{B}}^{\mathcal{V}} = \begin{bmatrix} \mathbf{R}_{\mathcal{B}}^{\mathcal{V}} & \mathbf{t}_{\mathcal{B}}^{\mathcal{V}} \\ 0 & 1 \end{bmatrix}, \quad \mathbf{T}_{\mathcal{E}}^{\mathcal{B}} = \begin{bmatrix} \mathbf{R}_{\mathcal{E}}^{\mathcal{B}} & \mathbf{t}_{\mathcal{E}}^{\mathcal{B}} \\ 0 & 1 \end{bmatrix} \quad (2)$$

where $\mathbf{R}_{\mathcal{V}}^{\mathcal{W}}$ and $\mathbf{t}_{\mathcal{V}}^{\mathcal{W}}$ are both obtained from VICON in this article. According to the CAD drawing, the $\mathbf{R}_{\mathcal{B}}^{\mathcal{V}}$ is an identity matrix and $\mathbf{t}_{\mathcal{B}}^{\mathcal{V}} = [0 \ 0 \ -d_{\mathcal{B}}^{\mathcal{V}}]^T$ indicates that only vertical translation $d_{\mathcal{B}}^{\mathcal{V}}$ occurs between \mathcal{V} and \mathcal{B} . The $\mathbf{T}_{\mathcal{E}}^{\mathcal{B}}$ can be calculated by the conventional tendon-length-based kinematics model [37] (constant curvature, i.e., CC) of the continuum robotic arm. In terms of the tendon actuation space \mathbf{L}_{cm} , its mapped configuration space is formed

$$\theta_{cm} r_{cm} \cos[\phi_{cm} + (i-1)\mu] = l_{cm} - l_i \quad (3)$$

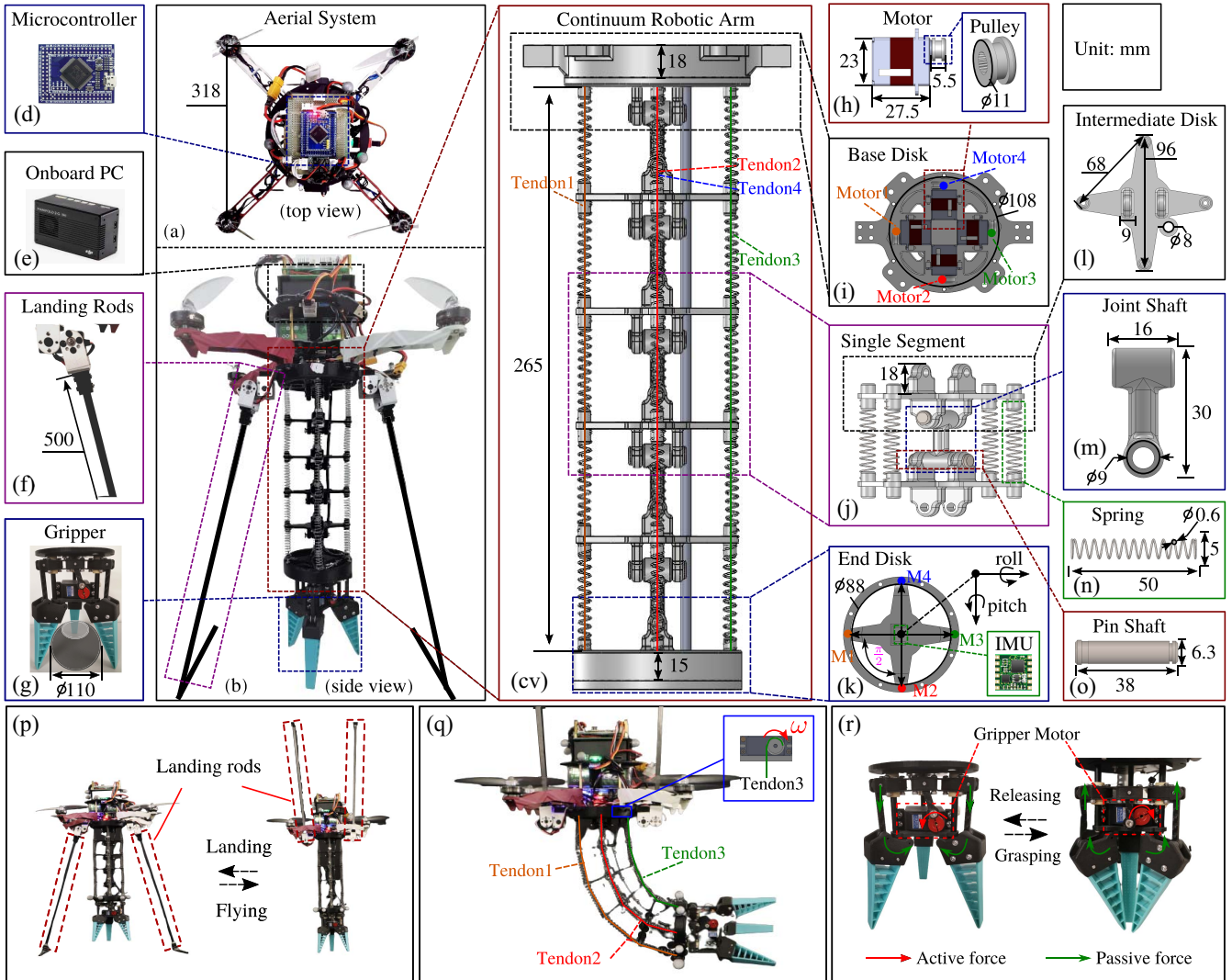


Fig. 4. Mechanical system architecture of the AeCoM. (a), (b) Side view and top view of the AeCoM in photography. (c) CAD drawing of the continuum robotic arm with tendons deployment. (d)–(g) Hardware components: a microcontroller as the central CPU for the robotic arm, an onboard PC as the main brain for the whole system, a pair of landing rods for supporting the system, and a gripper for aerial grasping. (c), (h)–(o) CAD drawings of the continuum robotic arm with its essential components. (k) IMU installation with “M1–M4” meaning the order of four tendon motors, and rotation axis configuration (pitch rotation driven by M1 and M3, roll rotation driven by M2 and M4). (p) Illustration for the workflow of landing rods. (q) Tendons state during aerial spatial motion, which is driven by an actuation motor in means of tendon winding. (r) Illustration for the workflow of the gripper.

where $i \in \{1, 2, 3, 4\}$ indicates the indexed tendons and $\mu = (\pi/2)$ denotes the interval radian between two adjacent tendons. Regarding to θ_{cm} and ϕ_{cm} , the translation and rotation components of the T_E^B can be calculated [38].

Unlike previous studies on the continuum robots, the AeCoM is required to cope with fast maneuvers and variable loading in different aerial manipulation tasks. The challenge is that fast maneuvers tend to cause tendon slacking and variable loading brings external disturbance. It leads to uncertain tendon lengths and nonconstant curvature for the continuum body, and the conventional model produces inestimable errors. Therefore, the authors propose an IMU-based continuum kinematic model to obtain the real time and more precise T_E^B under the aforementioned circumstances.

B. IMU-Based Continuum Kinematic Modeling

The curvature and stiffness of the continuum body are vulnerable to external loading. For the sake of high update

frequency and dynamics measurement, IMU sensors are implemented on the AeCoM to build a robust and precise kinematic model. One of the IMUs is embedded in the UAV flight controller board to provide the attitude estimation by the internal extended Kalman filter [9] for the UAV plane \mathcal{V} and the manipulator’s base plane \mathcal{B} , owing to two planes’ rigid connection.

The other IMU is installed in the EE plane \mathcal{E} to provide measurements of acceleration and angular velocity. The IMU sensor is modeled as [39]

$$\begin{aligned} \omega_m &= \hat{\omega} + b_g + \mu_g \\ \alpha_m &= R(\hat{\alpha} - g) + b_a + \mu_a \end{aligned} \quad (4)$$

where ω_m is the measured angular velocity and $\hat{\omega}$ is the ideal angular velocity. Also, α_m and $\hat{\alpha}$ represent the measured acceleration and ideal acceleration, respectively. b_g and b_a are random measurement bias that changes with time. μ_g and μ_a are zero-mean Gaussian white noise. R is the rotation

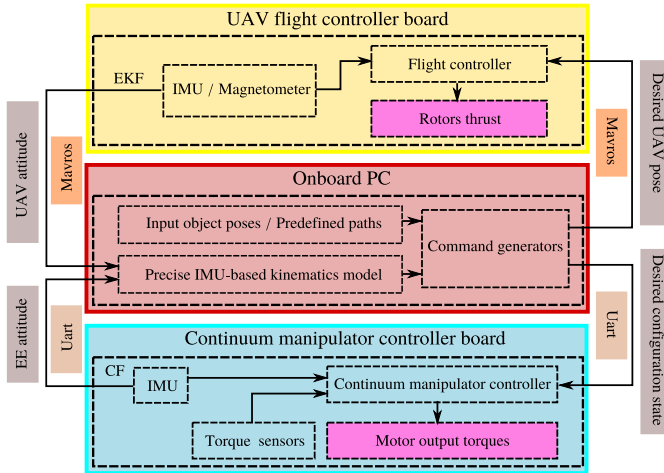


Fig. 5. AeCoM system running flow. The onboard PC serves as the core brain which receives multiple sensory measurements and generates maneuver commands. The UAV flight controller and continuum manipulator controller boards are responsible for their respective motion tasks.

matrix from the IMU frame to the world frame. \mathbf{g} is the gravity acceleration.

For readability, here, we discuss the attitude estimation of the EE frame. The authors use a complementary filter to fuse acceleration $\mathcal{E}\boldsymbol{\alpha}_{m,t}$ and angular velocity $\mathcal{E}\boldsymbol{\omega}_{m,t}$ measurements of the EE's IMU, to estimate the attitude of the EE frame $\mathcal{E}\boldsymbol{q}_t$ in quaternion manifold, with respect to the world frame \mathcal{W} . The right subscript t denotes the time within the filter update period. The filter starts with calculating orientation error by acceleration measurements, and the error from the previous estimation $\mathcal{W}\tilde{\boldsymbol{q}}_{est,t} = [q_w \ q_x \ q_y \ q_z]^T$ is given as

$$\begin{aligned} \mathbf{h}(\mathcal{E}\tilde{\boldsymbol{q}}_{est,t}) &= \begin{bmatrix} 2(q_x q_z - q_w q_y) \\ 2(q_w q_x + q_y q_z) \\ (q_w^2 - q_x^2 - q_y^2 + q_z^2) \end{bmatrix} \\ \mathbf{e}_{t+1} &= \mathcal{E}\tilde{\boldsymbol{\alpha}}_{m,t+1} \times \mathbf{h}(\mathcal{E}\tilde{\boldsymbol{q}}_{est,t}) \\ \mathbf{e}_{i,t+1} &= \mathbf{e}_t + \mathbf{e}_{t+1} \Delta t \end{aligned} \quad (5)$$

where the superscript $\tilde{\cdot}$ denotes the vector normalization. Δt is the time elapsed between two samples at t and $t+1$. $\mathbf{h}(\cdot)$ denotes the operation of gravity projection on the \mathcal{E} frame.

Then, the error by acceleration measurements is used to update gyro (angular velocity) measurements by compensation, given as

$$\mathcal{B}\boldsymbol{\omega}_{t+1} = \mathcal{B}\boldsymbol{\omega}_{m,t+1} + \mathbf{k}_p^\omega \mathbf{e}_{t+1} + \mathbf{k}_i^\omega \mathbf{e}_{i,t+1} \quad (6)$$

where \mathbf{k}_p^ω and \mathbf{k}_i^ω denote PI compensation gains. With corrected gyro measurements, the orientation increment from the sample t to $t+1$ is computed as

$$\mathcal{W}\dot{\boldsymbol{q}}_{\omega,t+1} = \frac{1}{2}\mathcal{E}\tilde{\boldsymbol{q}}_{est,t} \otimes \left[0, \mathcal{E}\boldsymbol{\omega}_{t+1} \right]^T \quad (7)$$

where \otimes denotes quaternion multiplication by the first-order Runge–Kutta method. At sample $t+1$, the sensor orientation is updated by integrating orientation increment

$$\mathcal{W}\boldsymbol{q}_{est,t+1} = \mathcal{W}\tilde{\boldsymbol{q}}_{est,t} + \mathcal{W}\dot{\boldsymbol{q}}_{\omega,t+1} \Delta t. \quad (8)$$

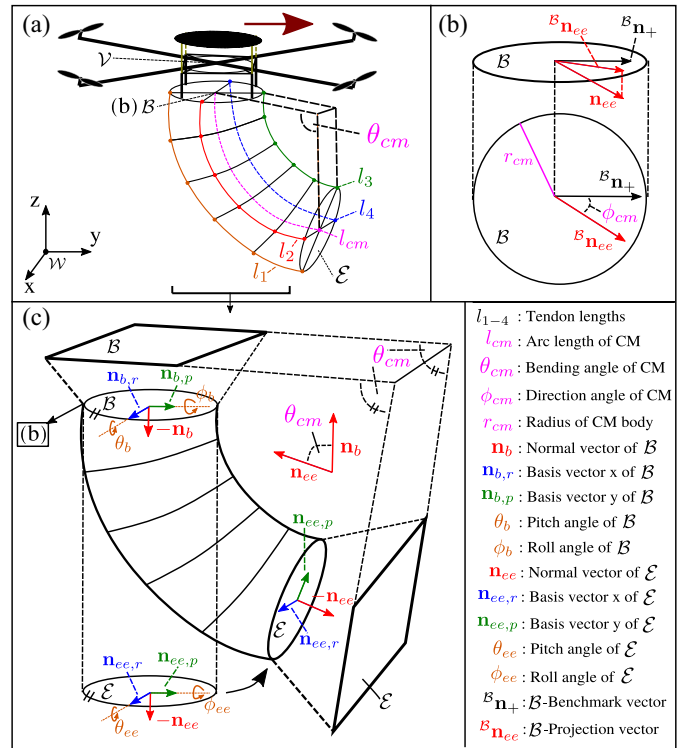


Fig. 6. AeCoM kinematics diagram with the detailed denotation of used variables. (a) Generalized system frames and configuration of the AeCoM. (b) Manipulator base frame \mathcal{B} with the plane benchmark vector and the projection vector of the EE plane's normal. (c) IMU-based continuum configuration with key vectors and variables generation.

With the complementary filtering, the Euler angles $\{\mathcal{W}\theta, \mathcal{W}\phi\}$ is obtained from the $\mathcal{W}\boldsymbol{q}_{est} = [q_{e,w} \ q_{e,x} \ q_{e,y} \ q_{e,z}]^T$.

Thanks to the mechanical constraints of joint shafts in Fig. 4, the twisting motion around its backbone direction could be neglected. It leads to a situation in which the IMU on the EE and the IMU on the UAV body, share the same inertial frame in the initial placement, as depicted in Fig. 6. Then, the authors employ the attitude information of the two IMUs to build the spatial relation between the base plane and the EE plane, in order further to derive the continuum configuration space λ_{cm} . Essentially, the relation between two planes could be described by their normal vectors. To derive the normal vectors, the attitude of the EE plane \mathcal{E} is denoted as θ_{ee} and ϕ_{ee} , and the attitude of the base plane \mathcal{B} is denoted as θ_b and ϕ_b . The basis unit vectors of the EE plane $[\mathbf{n}_{ee,r} \ \mathbf{n}_{ee,p}]^T$ and the base plane $[\mathbf{n}_{b,r} \ \mathbf{n}_{b,p}]^T$ are defined by the respective attitudes

$$\begin{aligned} \mathcal{E} : \begin{cases} \mathbf{n}_{ee,r} = [c(\phi_{ee}) \ 0 \ s(\phi_{ee})]^T \\ \mathbf{n}_{ee,p} = [0 \ c(\theta_{ee}) \ s(\theta_{ee})]^T \end{cases} \\ \mathcal{B} : \begin{cases} \mathbf{n}_{b,r} = [c(\phi_b) \ 0 \ s(\phi_b)]^T \\ \mathbf{n}_{b,p} = [0 \ c(\theta_b) \ s(\theta_b)]^T \end{cases} \end{aligned} \quad (9)$$

where the notation $c(\cdot)$ and $s(\cdot)$ denote $\cos(\cdot)$ and $\sin(\cdot)$ operations, respectively. The right subscripts r and p denote the roll axis and the pitch axis. The normal vectors of the two planes, \mathbf{n}_{ee} and \mathbf{n}_b are computed by cross multiplication

$$\begin{aligned} \mathbf{n}_{ee} &= \mathbf{n}_{ee,r} \times \mathbf{n}_{ee,p} \\ \mathbf{n}_b &= \mathbf{n}_{b,r} \times \mathbf{n}_{b,p}. \end{aligned} \quad (10)$$

Then, the included angle of the two planes is regarded as the bending angle θ_{cm} of the continuum body. Based on IMU sensors, the continuum configuration space is given as

$$\begin{aligned}\theta_{cm} &= \langle \mathbf{n}_{ee}, \mathbf{n}_b \rangle, \quad \theta \leq \frac{\pi}{2} \\ {}^B\mathbf{n}_{ee} &= \mathbf{n}_{ee} - (\mathbf{n}_{ee} \cdot \mathbf{n}_b) \cdot \mathbf{n}_b \\ \phi_{cm} &= \langle {}^B\mathbf{n}_{ee}, {}^B\mathbf{n}_+ \rangle, \quad \phi \leq 2\pi\end{aligned}\quad (11)$$

where the operation $\langle \cdot, \cdot \rangle$ denotes the included angle of two vectors, $|\mathbf{n}_{ee}| = |\mathbf{n}_b| = 1$, ${}^B\mathbf{n}_{ee}$ denotes the projection vector of the \mathbf{n}_{ee} in the base plane \mathcal{B} , and ${}^B\mathbf{n}_+$ is defined as the benchmark vector in the base plane \mathcal{B} . The direction angle ϕ_{cm} is derived by the included angle between the projection vector ${}^B\mathbf{n}_{ee}$ and the benchmark vector ${}^B\mathbf{n}_+$.

Regarding (11), a direct spatial relation is established between the \mathcal{B} and the \mathcal{E} by IMU sensors, without disturbance-vulnerable tendon lengths. With the configuration of the continuum part, the authors can derive the translation of the EE frame \mathcal{E} with respect to the base frame \mathcal{B} , as

$${}^B\mathbf{P}_{ee} = \begin{bmatrix} x_{ee} \\ y_{ee} \\ z_{ee} \end{bmatrix} = \frac{l_{cm}}{\theta_{cm}} \begin{bmatrix} (1 - \cos \theta_{cm}) \cos \phi_{cm} \\ (1 - \cos \theta_{cm}) \sin \phi_{cm} \\ \sin \theta_{cm} \end{bmatrix} \quad (12)$$

where l_{cm} denotes the approximated circular length. Inversely, to compute desired continuum configuration with the targeted translation, the inverse kinematics is given by

$$\begin{bmatrix} \theta_{cm} \\ \phi_{cm} \end{bmatrix} = \begin{bmatrix} 2 \arccos\left(\frac{|z_{ee}|}{\|{}^B\mathbf{P}_{ee}\|_2}\right) \\ \arctan\left(\frac{y_{ee}}{x_{ee}}\right) \end{bmatrix} \quad (13)$$

where $\|\cdot\|_2$ is the Euclidean norm.

Compared with the conventional kinematic model, the proposed model establishes a direct spatial relation between the \mathcal{B} and the \mathcal{E} by IMU measurements, instead of disturbance-vulnerable tendon lengths. Also, the local constant curvature assumption facilitates the solution of EE poses, under variable loading. The precision validation and comparison results of EE poses are presented in Section V.

IV. CONTROL

This section presents the control framework of the AeCoM system, which employs a decentralized control strategy and divides the whole system into two control subsystems: 1) the aerial platform controller and 2) the continuum manipulator controller. The fundamental application for the AeCoM is to actuate the EE under the proposed controller, to precisely approach a desired pose in the world frame. Considering the manipulator part as a tendon-driven robotic arm, the controller should be capable of coping with variable loading and fast maneuvering during consecutive motion. The control framework of the AeCoM system is designed to ensure precise and stable control of the continuum manipulator, even under varying loading and fast maneuvering.

A. UAV Controller

Given a desired object pose for the EE of the AeCoM, a controller is designed for the UAV platform to track the associated pose that is derived from the system's inverse kinematics.

Here, the UAV state is denoted by $X_u = \{\mathbf{p}_u, \mathbf{R}_u, \dot{\mathbf{p}}_u, \boldsymbol{\omega}_u\}$, including the UAV position $\mathbf{p}_u \in \mathbb{R}^3$, its rotation $\mathbf{R}_u = [r_x \ r_y \ r_z]$ ($\mathbf{R}_u \in SO(3)$), the linear velocity $\dot{\mathbf{p}}_u \in \mathbb{R}^3$, and the angular velocity $\boldsymbol{\omega}_u \in \mathbb{R}^3$. By this notation, the UAV dynamics model [40] can be derived by

$$\begin{cases} m\ddot{\mathbf{p}}_u = mg + f\mathbf{r}_z \\ \dot{\mathbf{R}}_u = \mathbf{R}_u\hat{\boldsymbol{\omega}}_u \\ J\hat{\boldsymbol{\omega}}_u = -\boldsymbol{\omega}_u \times J\boldsymbol{\omega}_u + \boldsymbol{\tau} + \boldsymbol{\tau}_{arm} \end{cases} \quad (14)$$

where m is the total mass of the AeCoM, \mathbf{g} is the gravity vector, J is the moment of inertia, f is the scalar thrust force (applied at the UAV center of mass and along the UAV vertical direction \mathbf{r}_z) resulting from the propeller forces f_1, f_2, f_3, f_4 , $\boldsymbol{\tau} \in \mathbb{R}^3$ is derived by the propeller forces, and $\boldsymbol{\tau}_{arm}$ is the torque exerted by the continuum robotic arm. In (14), the symbol \times is the vector cross product, the hat map $\hat{\cdot}$ maps a three-dimensional(3D) vector to a 3×3 skew-symmetric matrix, and its inverse operation, the vee map \cdot^\vee maps a 3×3 skew-symmetric matrix to a 3-D vector. The UAV controller takes input from a desired state $X^*_u = \{\mathbf{p}_{u,d}, \mathbf{R}_{u,d}, \dot{\mathbf{p}}_{u,d}, \boldsymbol{\omega}_{u,d}\}$ and computes the tracking errors [40]

$$\begin{aligned}\mathbf{e}_{u,p} &= \mathbf{p}_{u,d} - \mathbf{p}_u \quad (\text{positionerror}) \\ \mathbf{e}_{u,v} &= \dot{\mathbf{p}}_{u,d} - \dot{\mathbf{p}}_u \quad (\text{linear-velocityerror}) \\ \mathbf{e}_{u,R} &= \frac{1}{2}(\mathbf{R}_{u,d}^T \mathbf{R}_{u,d} - \mathbf{R}_{u,d}^T \mathbf{R}_u)^\vee \quad (\text{rotationerror}) \\ \mathbf{e}_{u,\omega} &= \mathbf{R}_{u,d}^T \mathbf{R}_{u,d} \boldsymbol{\omega}_{u,d} - \boldsymbol{\omega}_u \quad (\text{angular-velocityerror}).\end{aligned}\quad (15)$$

Then, the controller computes suitable thrust force f and torques $\boldsymbol{\tau}$ to eliminate these errors by using the control law

$$\begin{aligned}f &= -\mathbf{r}_z^T (k_{u,p} \mathbf{e}_p + k_{u,v} \mathbf{e}_v + mg - m\ddot{\mathbf{p}}_{u,d}) \\ \boldsymbol{\tau} &= -k_{u,R} \mathbf{e}_{u,R} - k_{u,\omega} \mathbf{e}_{u,\omega} + \boldsymbol{\omega}_u \times J\boldsymbol{\omega}_u \\ &\quad - J(\hat{\boldsymbol{\omega}}_u \mathbf{R}_{u,d}^T \mathbf{R}_{u,d} \boldsymbol{\omega}_{u,d} - \mathbf{R}_{u,d}^T \mathbf{R}_{u,d} \dot{\boldsymbol{\omega}}_{u,d})\end{aligned}\quad (16)$$

where $k_{u,p}$, $k_{u,v}$, $k_{u,R}$, and $k_{u,\omega}$ are tuned control gains. The controller enables the AeCoM to implement accurate positioning and trajectory tracking motion, which will be validated in Section V. Also, the controller stability has been proved in the AM [8]. In other words, the UAV controller copes with the majority of translational movements of the AeCoM, while precise object interaction requires the engagement of the manipulator controller.

B. Continuum Manipulator Controller

Considering the existence of the inertial moment between the segments, and inherent material factors, such as inhomogeneous stiffness and structural interference, the continuum manipulator cannot behave exactly as predicted by the dynamic model.

To implement the manipulator control, it is fundamental to control the pose of the EE. Given a targeted pose \mathbf{p}_t , the authors transfer it to the desired configuration space by the inverse kinematics (13). In Fig. 7, the current configuration space λ_{cm} is transformed to a config vector ${}^B\mathbf{v}_\lambda$, i.e., the projection vector of the EE's normal vector in the base plane \mathcal{B}

$${}^B\mathbf{v}_\lambda = |\mathbf{n}_\lambda| [c(\theta_{cm})s(\phi_{cm}) \ c(\theta_{cm})c(\phi_{cm})]^T \quad (17)$$

$${}^B\mathbf{v}_{\lambda,d} = |\mathbf{n}_\lambda| [c(\theta_{cm,d})s(\phi_{cm,d}) \ c(\theta_{cm,d})c(\phi_{cm,d})]^T \quad (18)$$

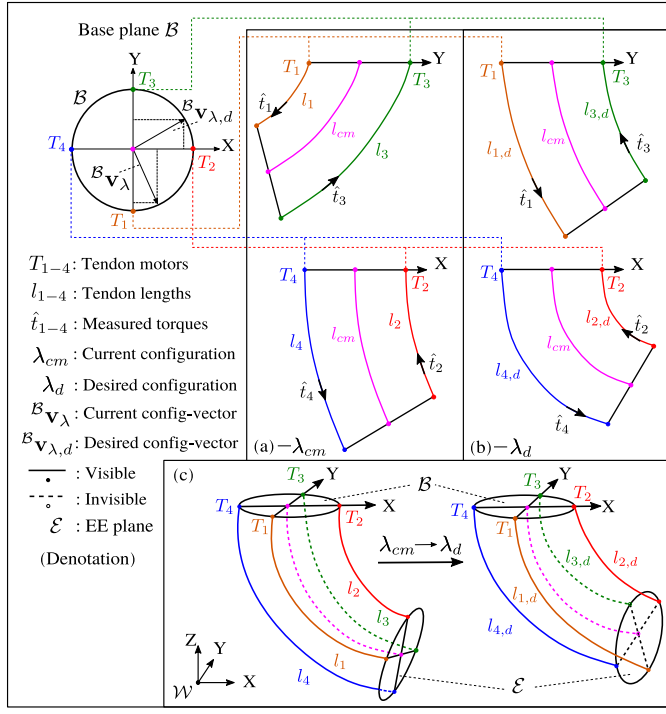


Fig. 7. Exampled configuration space transition process from the current state to the desired state, with the denotation of variables. In the manipulator base plane \mathcal{B} , both current and desired configuration states are projected as $\mathcal{B}v_{\lambda}$ (related to λ_{cm}) and $\mathcal{B}v_{\lambda,d}$ (related to λ_d). (a), (b) Corresponding individual y-axis plane formed by T_1 and T_3 tendons, and individual x-axis plane formed by T_2 and T_4 tendons, for current λ_{cm} and desired λ_d config states. (c) Overview of configuration states transition from the λ_{cm} to λ_d .

where $|\mathbf{n}_{\lambda}| = 1$ denotes the normal vector of the EE plane, and we denote the $\theta_{cm,d}$ and $\phi_{cm,d}$ with the subscript d as desired config values. Similarly, the desired config vector is denoted as $\mathcal{B}v_{\lambda,d}$ with the same composition. Then, their error vector $\mathcal{B}\mathbf{e}_{\lambda}$ is given as

$$\mathcal{B}\mathbf{e}_{\lambda} = \begin{bmatrix} \mathbf{e}_{\lambda,x} \\ \mathbf{e}_{\lambda,y} \end{bmatrix} = |\mathbf{n}_{\lambda}| \begin{bmatrix} c(\theta_{cm,d})s(\phi_{cm,d}) - c(\theta_{cm})s(\phi_{cm}) \\ c(\theta_{cm,d})c(\phi_{cm,d}) - c(\theta_{cm})c(\phi_{cm}) \end{bmatrix} \quad (19)$$

where $\mathbf{e}_{\lambda,x}$ is located on the x -axis formed by tendon motors (T_2 , T_4), and $\mathbf{e}_{\lambda,y}$ is located on the y -axis formed by tendon motors (T_1 , T_3), as shown in Fig. 7. $\mathcal{B}\mathbf{e}_{\lambda}$ maps the deviation between the desired configuration and the current configuration, into the actuation space. The conventional controllers [13], [14], [15] control the changing actuation lengths ΔL_{cm} , given by

$$\Delta L_{cm} = [\Delta l_1 \quad \Delta l_2 \quad \Delta l_3 \quad \Delta l_4]^T = k_{\lambda} \mathbf{E}_{\lambda} \quad (20)$$

$$\mathbf{E}_{\lambda} = [\mathbf{e}_{\lambda,y} \quad -\mathbf{e}_{\lambda,x} \quad -\mathbf{e}_{\lambda,y} \quad \mathbf{e}_{\lambda,x}]^T$$

where k_{λ} is the scaling coefficient and \mathbf{E}_{λ} is the configuration error matrix. Thus, given an expected λ_d , the corresponding ΔL_{cm} can be achieved by open-loop controlling related actuation motors with embedded encoders. Many studies in [12] have implemented the open-loop control approach on continuum robots. However, they cannot provide enough motion accuracy during fast and continuous maneuvers, also with external disturbance. The experimental performance of the conventional controller is presented in Fig. 10, Section V.

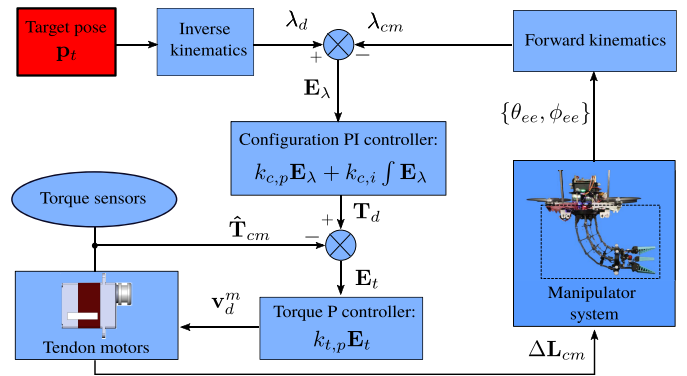


Fig. 8. Overview of the closed-loop kinematic controller for the continuum manipulator. The torque sensors are embedded into the tendon motors, and provide torque measurements \hat{T}_{cm} applied on tendons.

Instead of the conventional control method (directly achieving ΔL_{cm}), we consider a configuration-feedback approach to implement real-time closed-loop control. A PI control law can be derived as follows:

$$\mathbf{v}_d^m = [v_{1,d}^m \quad v_{2,d}^m \quad v_{3,d}^m \quad v_{4,d}^m]^T = k_{c,p} \mathbf{E}_{\lambda} + k_{c,i} \int \mathbf{E}_{\lambda} \quad (21)$$

where $k_{c,p}$ and $k_{c,i}$ are the closed-loop control gains. \mathbf{v}_d^m denotes the desired actuation velocity of the tendon motors.

However, if internal friction and variable loading are involved, these disturbances cause asymmetric force distribution on actuation tendons. Also, it is difficult to build a model to estimate the force distribution. Thus, the controller (21) is not able to compute the appropriate desired velocity for tendon motors, only relying on the config feedback. Under this case, tendon slacking tends to occur (Fig. 10, Section V). To tackle the unknown force distribution, we utilize the torque sensors embedded in the tendon motors to obtain the measurements of tension applied on corresponding tendons

$$\hat{T}_m = f_t \cdot \hat{r}_m \quad (22)$$

where \hat{T}_m denotes the measured torque outputted by one motor, \hat{r}_m is the estimated radius of the connected pulley, and f_t denotes the tension on the corresponding tendon. The torque measurements could be used to monitor the tension distribution. Therefore, the authors propose a two-loop controller with its structure shown in Fig. 8.

$\hat{\mathbf{T}}_{cm} = [\hat{t}_1 \quad \hat{t}_2 \quad \hat{t}_3 \quad \hat{t}_4]^T$ is denoted as the torque measurement vector shown in Fig. 7, and the desired torque vector is defined as $\mathbf{T}_d = [t_{1,d} \quad t_{2,d} \quad t_{3,d} \quad t_{4,d}]^T$. The desired torque vector is aimed at restraining the balance of tendon tension, to further reduce the possibility of tendon slacking. To achieve this, the relations $|t_{1,d}| \approx |t_{3,d}|$ and $|t_{2,d}| \approx |t_{4,d}|$ are expected for the y-axis plane and the x-axis plane, as shown in Fig. 7. The outer-loop control law can be designed as follows:

$$\mathbf{T}_d = k_{c,p} \mathbf{E}_{\lambda} + k_{c,i} \int \mathbf{E}_{\lambda} \quad (23)$$

where the PI controller output for correction of the configuration state error, satisfies the desired torque relation for y-axis, and x-axis planes. Then, we build the torque error vector

$$\mathbf{E}_t = \mathbf{T}_d - \hat{\mathbf{T}}_{cm} \quad (24)$$

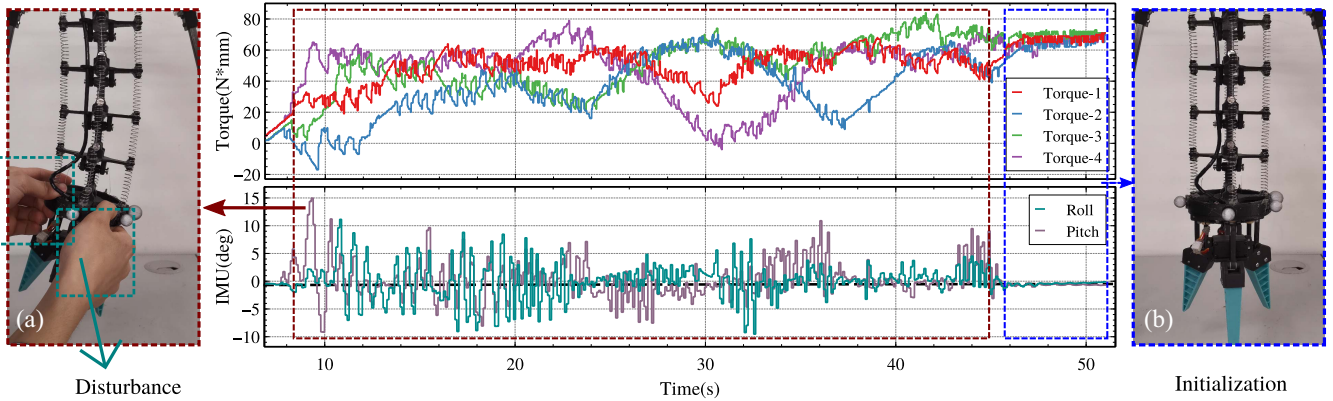


Fig. 9. Digital process of the system initialization. (a) Disturbance stage: external intervention is put on the robotic arm. (b) Initialization process is finished.

Then, an inner P controller is used to reduce the torque error E_t to prevent tendon slacking

$$v_d^m = k_{t,p} E_t \quad (25)$$

where $k_{t,p}$ denotes the inner control gains. Thus, involving torque feedback, the updated cascaded PI controller is formed as

$$v_d^m = k_{t,p} \left[\left(k_{c,p} E_\lambda + k_{c,i} \int E_\lambda \right) - \hat{T}_{cm} \right]. \quad (26)$$

In this section, authors discuss the relation between the tendon actuation mechanism and the configuration state of the continuum manipulator, by an example of the config transition shown in Fig. 7. Meanwhile, based on the actuation mechanism, a closed-loop kinematic controller is proposed with configuration state and torque feedback to implement robust and fast locomotion. More importantly, by the proposed controller, actual loading-lifting experiments are conducted to validate the performance of tendon slacking prevention in Section V-C.

V. EXPERIMENTS AND RESULTS

This section presents a comprehensive evaluation of the proposed aerial system including five interconnected aspects. The arrangement of the experiments is set as system initialization for keeping tendons pretension, payload capacity validation during flights, robotic arm controller for IMU-feedback spatial motion and tendon-slacking prevention, validation of the kinematics model for computing accurate EE poses with respect to the UAV frame, and aerial grasping for actual objects.

A. Automatic System Initialization

For all tendon-driven continuum robots, it is crucial to initialize the displacement of the continuum body and the tension in the tendons. Previous methods involving manual tightening or mechanical structures for pretensioning, which are feasible but tedious and time consuming [13], [14]. In the proposed AeCoM, the initialization process is simplified with the use of torque sensors and an IMU to implement an automatic self-initialization method. This ensures that the continuum robotic

arm adjusts to the perfect attitude quickly, with the EE plane parallel to the horizontal plane. The attitude-adjust control frequency is set at 5 ms, and each tendon is automatically straightened with an equivalent torque measurement, without any manual or mechanical assistance. This simplification of the initialization process in the proposed AeCoM not only saves time but also improves the accuracy and efficiency of the initialization process, making it more practical for real-world applications.

Fig. 9 demonstrates the real-time variation of four tendons' torque measurements and the attitude of the EE plane during a random initialization process, with aggressive intervention imposed to test the robustness of the initialization process. The figure shows that a 30-s external intervention changes the attitude aggressively, with fluctuating roll and pitch angles and violent torque measurements. However, during the last 10 s, the four tendons' torque measurements converge to the same value, and the EE's attitude reaches the expected state with roll and pitch angles nearly to 0°. To prove the repeatability, the authors conduct the method more than 20 times with different duration of the disturbance, and all tests achieve the same expected result. This experiment indicates that the proposed initialization method enables the whole system to self-initialize automatically, even when suffering aggressive disturbance, demonstrating its robustness and repeatability.

B. Payload Capacity Validation

Payload capacity is an important factor for evaluating an aerial manipulation system. For versatile aerial manipulation tasks, it is inevitable to deal with variable loading, such as different devices on the EE or various interaction objects. To evaluate the payload capacity, it is necessary to determine the maximum limit of loading, considering both the UAV platform and the robotic arm. In experimental flights, authors increase the loading from 0 to 500 g to test the maximum limit by the continuum manipulator, which weighs only 60 g. The AeCoM flies to a certain height and hovers, and a single-axis spatial motion (pitch: 0° to 90°) of the robotic arm is conducted to test the lifting capability. Fig. 11 shows the test result with a 500-g loading. The desired bending angle is set as 90°, and the controller changes the shape of the robotic arm to make

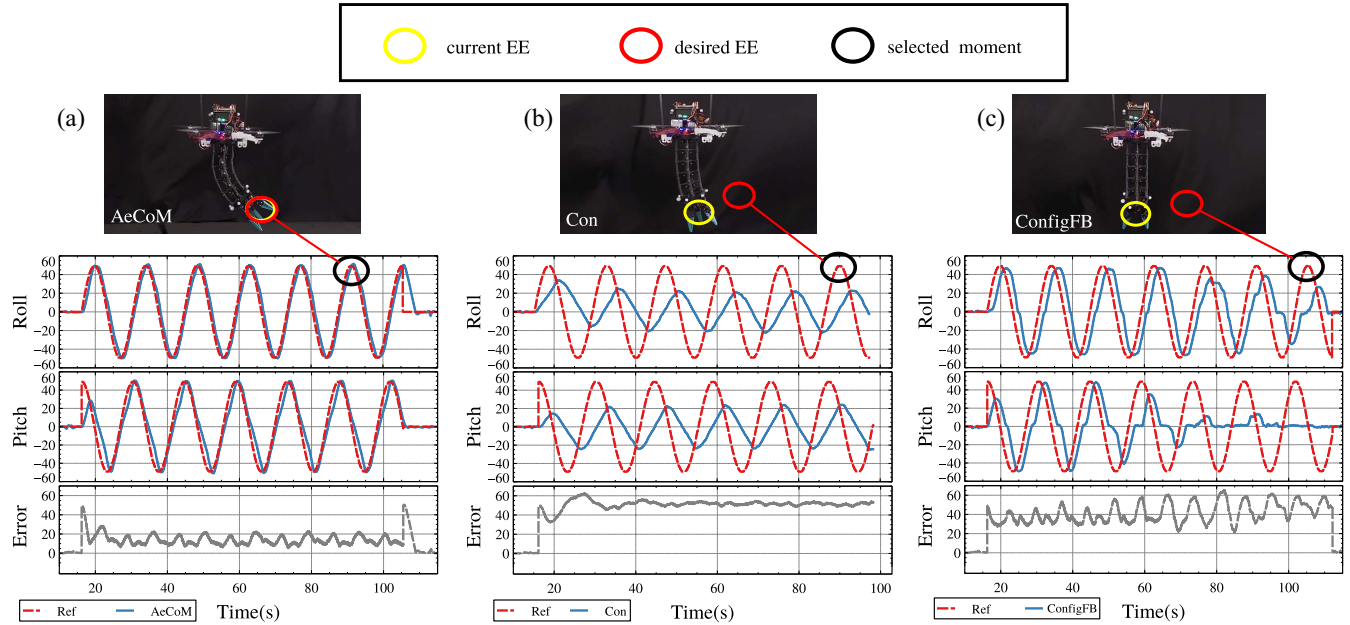


Fig. 10. Comparison result (unit: degree) between three controllers for EE attitude control, during the aerial dual-axis spatial motion. (a) Proposed controller (AeCoM) has the lowest attitude tracking error. (b) Conventional controller (Con). (c) Config-feedback controller (ConfigFB). The red dashed line represents the ground truth. A moment during the flight is selected to check the status of the current EE and desired EE.

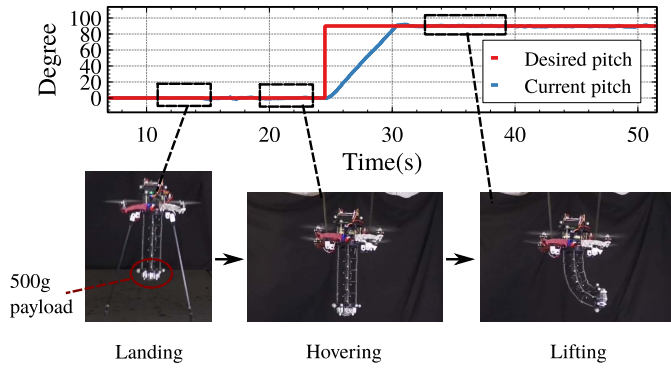


Fig. 11. 500-g loading test of the system during hovering flights, with screenshots of different states: landing, hovering, and lifting.

the current angle achieve the expected angle. This evaluation proves that the proposed aerial system can lift at least a weight of 500 g during aerial manipulation, demonstrating its strong payload capacity for various aerial manipulation tasks.

C. Tendon-Slacking Prevention Controller Evaluation

To cope with complex aerial application tasks, the proposed system is required to have a delicate motion response. Experiments of aerial fast motion are designed to validate the capability of slacking avoidance. During hovering flights, the AeCoM conducts consecutive swing motion in a large spatial range, following the pitch and roll axis -90° to 90° , respectively, with a loading of 260 g, which is the weight of the gripper. The discrepancy between the current attitude and desired attitude should be limited to an extremely low value to prove that no slacking occurred during the aggressive motion. In other words, if the current attitude cannot track the desired attitude, it is evident that the tendons cannot provide sufficient

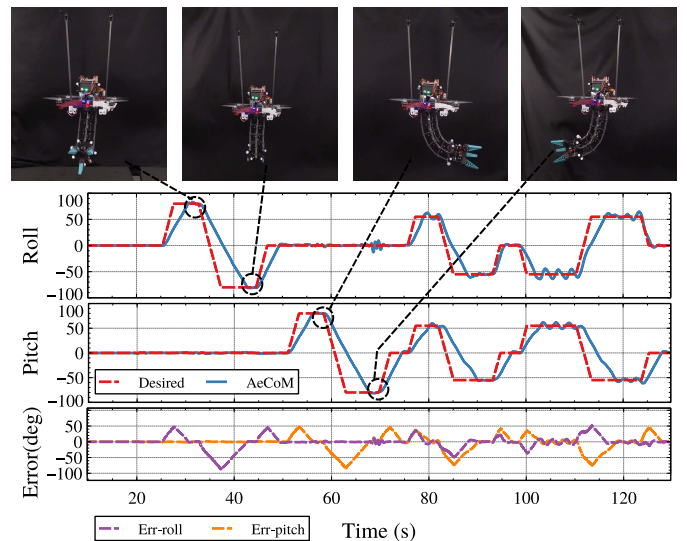


Fig. 12. Consecutive spatial motion of the robotic arm both on the pitch axis and roll axis during an aerial flight with the loading of 260 g. The EE's attitude tracks the desired attitude in real time.

and correct actuation to manipulate the continuum body, and tendon slacking occurs. This evaluation validates the capability of the proposed system in avoiding tendon slacking during aerial fast motion, which is vital for conducting complex aerial manipulation tasks.

Fig. 12 presents the real-time discrepancy between the desired attitude and the current attitude of the EE during the designed consecutive motion. The maximum angular velocity is 0.52 rad/s, and the error fluctuates around 0° during the whole consecutive motion with the 260-g loading, indicating that the motion is conducted successfully without any tendon slacking. To further prove the feasibility and

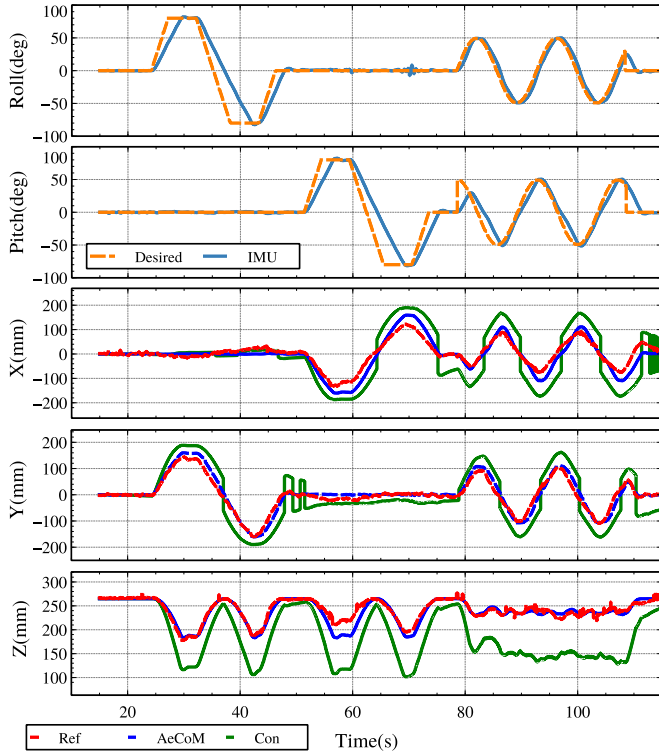


Fig. 13. Proposed kinematics model evaluation with the comparison with the conventional kinematics model, under the 300-g loading. The $X-Y-Z$ coordinates denote the translation of the EE frame relative to the AeCoM base frame. The red line as ground truth is derived from the VICON. The blue line and green line are computed by the proposed kinematic model and the conventional one.

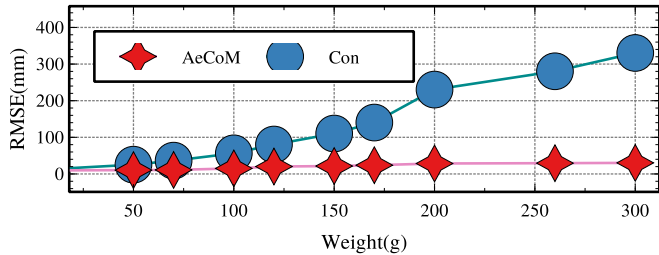


Fig. 14. RMSE of the proposed kinematics model (AeCoM) and the conventional model (Con) under variable loadings.

performance of the proposed manipulator controller, a continuous swing motion test is conducted using the designed controller, config-feedback controller, and the conventional continuum controller. The experimental motion is defined as a continuous dual-axis swing motion within the range of 50° during hovering flights, with an overall loop frequency of 4 ms for each controller. The comparison result of these three controllers for attitude control is shown in Fig. 10. This experiment demonstrates the superior attitude control performance of the proposed manipulator controller compared to the config-feedback controller and the conventional continuum controller.

The experiment compares three controllers under a predefined motion. The proposed controller and the config-feedback PI controller have similar performance on attitude

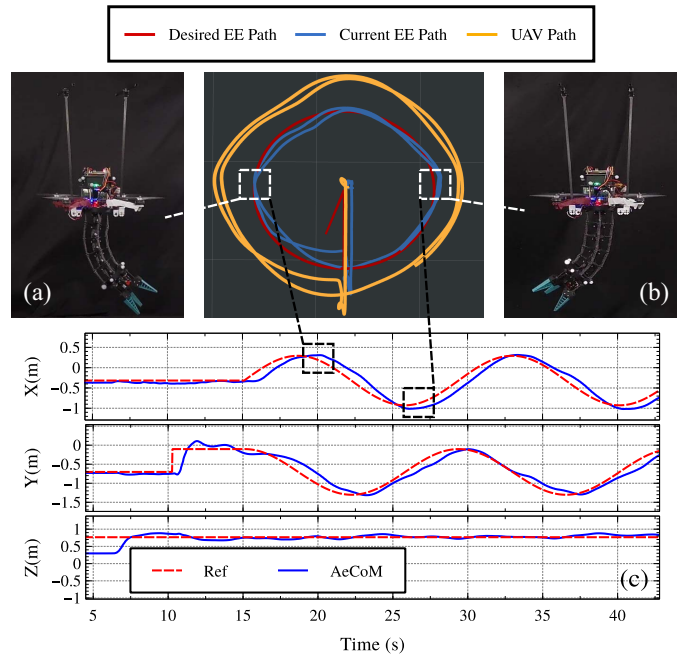


Fig. 15. EE tracking motion in the world frame. (a) and (b) Show two selected moments during the tracking maneuver. (c) Red dashed curves denote the desired EE's global translation, while blue solid curves show the real-time EE's global translation $X-Y-Z$.

tracking during the first several periods, with similar response rates and fitting curves. However, the config-feedback PI controller loses the capability of tracking due to tension loss without torque feedback. The proposed controller maintains stable and robust tracking performance. Additionally, the comparison between the proposed controller and the conventional continuum controller shows that the latter cannot handle fast-tracking motion. This comparison highlights the advantages of the proposed controller in maintaining stable and accurate tracking performance, even under challenging conditions.

D. Precise Kinematics Modeling Validation

Validating the accuracy of the designed kinematics model is challenging. The translational part is the key factor that determines the relative position of the EE with regard to the UAV body frame. To evaluate the proposed kinematic model, we utilize the VICON system to obtain the poses of both the UAV and the EE. The discrepancy between the VICON system and the proposed model is regarded as the translational measurement in the ground truth. The single-axis spatial motion along the roll (-90° to 90°) and pitch (-90° to 90°) axis, and the dual-axis swing motion are conducted to evaluate the proposed kinematics model. During the whole spatial motion, the proposed kinematics model and conventional model produce translational solutions in $X-Y-Z$. The results of the two models are compared with the VICON ground truth under the loading of 300 g, as shown in Fig. 13. This evaluation validates the accuracy of the proposed kinematics model in determining the translational accuracy of the EE.

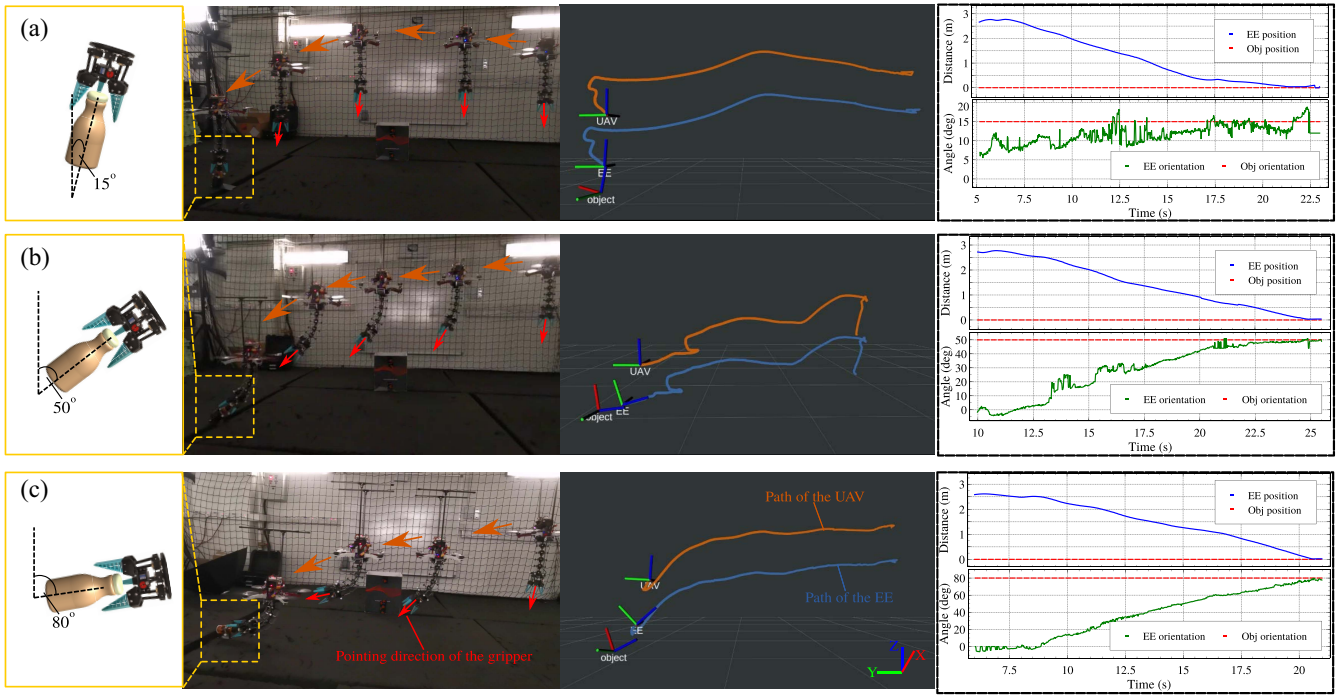


Fig. 16. Aerial grasping experiment for three grasping angles (15° , 50° , 80°) of the targeted bottle. The pointing direction of the gripper is marked in the flight screenshots. Paths and tf-coordinates of the UAV and EE are recorded to demonstrate the automatic aerial grasping process in Rviz.

To demonstrate the accuracy of the proposed kinematics model under different loading, a group of different weights is added to the EE. The root mean square error (RMSE) is computed to present the accuracy of the proposed model and the conventional model. The RMSE of both models with regard to weight is depicted in Fig. 14. The RMSE results show that, with the increase of weight, the RMSE of the proposed model is limited to 30 mm, while the RMSE of the conventional model reaches around 350 mm under 300 g. The results prove that the proposed model provides stable and satisfactory translational accuracy for the EE during consecutive spatial motions, and is more accurate than the conventional model under different loading conditions.

The kinematics model enables the computation of the real-time pose of the EE in the world frame with known global UAV poses, which is vital for actual interaction with the surroundings during aerial manipulation tasks. A tracking flight maneuver with a predefined trajectory is designed to evaluate the EE positioning and tracking performance. During the tracking flight, the UAV and the manipulator conduct movements simultaneously. The desired path and the AeCoM's path are recorded, and real-time translational data of the EE is presented in Fig. 15. This experiment validates the accuracy of the kinematics model in determining the EE's pose in real time.

E. Aerial Grasping

To validate the comprehensive functionality of the AeCoM, the authors design aerial grasping experiments. The aerial grasping is a challenge for payload capacity, the accuracy of the kinematics model, and the AeCoM controller. A bottle is

chosen as the target object, because it is easy to change its orientation. The designed experimental process includes the grasping stage, the placing stage, and the return stage. During the grasping stage, the AeCoM flies from a distant point to the object point. Meanwhile, the manipulator changes its orientation gradually to align with the object's orientation. When the gripper reaches the object, the gripper's pose should be equal to the object's pose. After the grasping stage, the AeCoM takes the object to a predefined position where a basket is put and drops the object. Then, the AeCoM returns to the original starting point.

Fig. 16 presents the aerial grasping stage with complete maneuver details, where objects are placed at three lean angles of 15° , 50° , and 80° . Each object angle is tested more than 10 times, and the average final error of the translation part is less than 3 mm, while the error in the orientation part is less than 0.05° . The average grasping duration is around 15 s. The experiments validate the adaptability of the AeCoM to variable object poses. After many grasping tests, the tendon-slacking situation never happens, which verifies the robustness of the tendon-slacking prevention. The precise kinematics model ensures the accurate gripper's pose, which is the key to successful aerial grasping. The aerial grasping experiment is a holistic aerial application, and the AeCoM fulfills the maneuver requirements with the validation of the proposed methods.

VI. CONCLUSION

The article proposes a novel AeCoM, called AeCoM, with original mechanical design, complete modeling, and control framework. The AeCoM has better payload capacity and

motion flexibility compared to previous aerial rigid manipulators, as well as higher system completeness and manipulation capability than other AeCoMs. The article addresses the issue of tendon slacking in the tendon-driven continuum robotic arm by designing a robust controller with IMU and torque feedback, and establishes a novel IMU-based kinematics model for the proposed aerial system under external loading. Comprehensive experiments are conducted to validate the performance of the AeCoM, including actual aerial flights with the robotic arm's motion, automatic initialization method for the continuum robotic arm, evaluation of payload capacity with variable loading during aerial spatial motion, and validation of the robotic arm's controller. The AeCoM shows good accuracy in kinematics modeling and aerial grasping tasks, and has potential for future applications.

REFERENCES

- [1] F. Ruggiero, V. Lippiello, and A. Ollero, "Aerial manipulation: A literature review," *IEEE Robot. Autom. Lett.*, vol. 3, no. 3, pp. 1957–1964, Jul. 2018.
- [2] D. Lee, H. Seo, D. Kim, and H. J. Kim, "Aerial manipulation using model predictive control for opening a hinged door," in *Proc. IEEE Int. Conf. Robot. Autom.*, Paris, France, 2020, pp. 1237–1242.
- [3] H. Chen, F. Quan, L. Fang, and S. Zhang, "Aerial grasping with a lightweight manipulator based on multi-objective optimization and visual compensation," *Sensors*, vol. 19, no. 19, p. 4253, 2019.
- [4] M. Tognon et al., "A truly-redundant aerial manipulator system with application to push-and-slide inspection in industrial plants," *IEEE Robot. Autom. Lett.*, vol. 4, no. 2, pp. 1846–1851, Apr. 2019.
- [5] M. Cai, Y. Wang, S. Wang, R. Wang, L. Cheng, and M. Tan, "Prediction-based seabed terrain following control for an underwater vehicle-manipulator system," *IEEE Trans. Syst., Man, Cybern., Syst.*, vol. 51, no. 8, pp. 4751–4760, Aug. 2021.
- [6] A. Suarez, G. Heredia, and A. Ollero, "Physical-virtual impedance control in ultralightweight and compliant dual-arm aerial manipulators," *IEEE Robot. Autom. Lett.*, vol. 3, no. 3, pp. 2553–2560, Jul. 2018.
- [7] M. J. Kim, R. Balachandran, M. De Stefano, K. Kondak, and C. Ott, "Passive compliance control of aerial manipulators," in *Proc. IEEE/RSJ Int. Conf. Intell. Robots Syst.*, Madrid, Spain, 2018, pp. 4177–4184.
- [8] L. Fang, H. Chen, Y. Lou, Y. Li, and Y. Liu, "Visual grasping for a lightweight aerial manipulator based on NSGA-II and kinematic compensation," in *Proc. IEEE Int. Conf. Robot. Autom.*, Brisbane, QLD, Australia, 2018, pp. 3488–3493.
- [9] F. Pierri, G. Muscio, and F. Caccavale, "An adaptive hierarchical control for aerial manipulators," *Robotica*, vol. 36, no. 10, pp. 1527–1550, 2018.
- [10] K. M. Popek et al., "Autonomous grasping robotic aerial system for perching (AGRASP)," in *Proc. IEEE/RSJ Int. Conf. Intell. Robots Syst.*, Madrid, Spain, 2018, pp. 1–9.
- [11] R. Peng, X. Chen, and P. Lu, "A motion decoupled aerial robotic manipulator for better inspection," in *Proc. IEEE/RSJ Int. Conf. Intell. Robots Syst.*, Prague, Czech Republic, 2021, pp. 4207–4213.
- [12] X. Meng, Y. He, and J. Han, "Survey on aerial manipulator: System, modeling, and control," *Robotica*, vol. 38, no. 7, pp. 1288–1317, 2020.
- [13] R. J. Webster, III and B. A. Jones, "Design and kinematic modeling of constant curvature continuum robots: A review," *Int. J. Robot. Res.*, vol. 29, no. 13, pp. 1661–1683, 2010.
- [14] S. Kolachalam and S. Lakshmanan, "Continuum robots for manipulation applications: A survey," *J. Robot.*, vol. 2020, Jul. 2020, Art. no. 4187048.
- [15] Z. Samadikhoshkho, S. Ghorbani, and F. Janabi-Sharifi, "Modeling and control of aerial continuum manipulation systems: A flying continuum robot paradigm," *IEEE Access*, vol. 8, pp. 176883–176894, 2020.
- [16] J. L. Chien, L. T. L. Clarissa, J. Liu, J. Low, and S. Foong, "Kinematic model predictive control for a novel tethered aerial cable-driven continuum robot," in *Proc. IEEE/ASME Int. Conf. Adv. Intell. Mechatronics*, Delft, The Netherlands, 2021, pp. 1348–1354.
- [17] Q. Zhao, G. Zhang, H. Jafarnejadsani, and L. Wang, "A modular continuum manipulator for aerial manipulation and perching," 2022, *arXiv:2206.06246*.
- [18] R. Szász, M. Allenspach, M. Han, M. Tognon, and R. K. Katzschmann, "Modeling and control of an omnidirectional micro aerial vehicle equipped with a soft robotic arm," in *Proc. IEEE Int. Conf. Soft Robot.*, Edinburgh, U.K., 2022, pp. 1–8.
- [19] D. Bruder, X. Fu, R. B. Gillespie, C. D. Remy, and R. Vasudevan, "Koopman-based control of a soft continuum manipulator under variable loading conditions," *IEEE Robot. Autom. Lett.*, vol. 6, no. 4, pp. 6852–6859, Oct. 2021.
- [20] F. Feng, W. Hong, and L. Xie, "A learning-based tip contact force estimation method for tendon-driven continuum manipulator," *Sci. Rep.*, vol. 11, no. 1, pp. 1–11, 2021.
- [21] F. Campisano et al., "Online disturbance estimation for improving kinematic accuracy in continuum manipulators," *IEEE Robot. Autom. Lett.*, vol. 5, no. 2, pp. 2642–2649, Apr. 2020.
- [22] É. Picard, S. Caro, F. Claveau, and F. Plestan, "Pulleys and force sensors influence on payload estimation of cable-driven parallel robots," in *Proc. IEEE/RSJ Int. Conf. Intell. Robots Syst.*, Madrid, Spain, 2018, pp. 1429–1436.
- [23] Y. Lin, H. Zhao, and H. Ding, "External force estimation for industrial robots with flexible joints," *IEEE Robot. Autom. Lett.*, vol. 5, no. 2, pp. 1311–1318, Apr. 2020.
- [24] G. Gao, H. Wang, Q. Xia, M. Song, and H. Ren, "Study on the load capacity of a single-section continuum manipulator," *Mech. Mach. Theory*, vol. 104, pp. 313–326, Oct. 2016.
- [25] X. Gao, X. Li, Y. Sun, L. Hao, H. Yang, and C. Xiang, "Model-free tracking control of continuum manipulators with global stability and assigned accuracy," *IEEE Trans. Syst., Man, Cybern., Syst.*, vol. 52, no. 2, pp. 1345–1355, Feb. 2022.
- [26] T. Liu, T. Yang, W. Xu, G. Mylonas, and B. Liang, "Efficient inverse kinematics and planning of a hybrid active and passive cable-driven segmented manipulator," *IEEE Trans. Syst., Man, Cybern., Syst.*, vol. 52, no. 7, pp. 4233–4246, Jul. 2022.
- [27] Z. Mu, Y. Chen, Z. Li, H. Qian, and N. Ding, "A spatial biarc method for inverse kinematics and configuration planning of concentric cable-driven manipulators," *IEEE Trans. Syst., Man, Cybern., Syst.*, vol. 52, no. 7, pp. 4177–4186, Jul. 2022.
- [28] D. B. Camarillo, C. R. Carlson, and J. K. Salisbury, "Configuration tracking for continuum manipulators with coupled tendon drive," *IEEE Trans. Robot.*, vol. 25, no. 4, pp. 798–808, Aug. 2009.
- [29] D. B. Camarillo, C. R. Carlson, and J. K. Salisbury, "Task-space control of continuum manipulators with coupled tendon drive," in *Proc. 11th Int. Symp. Exp. Robot.*, 2009, pp. 271–280.
- [30] A. Bajo, R. E. Goldman, and N. Simaan, "Configuration and joint feedback for enhanced performance of multi-segment continuum robots," in *Proc. IEEE Int. Conf. Robot. Autom.*, Shanghai, China, 2011, pp. 2905–2912.
- [31] R. S. Penning, J. Jung, N. J. Ferrier, and M. R. Zinn, "An evaluation of closed-loop control options for continuum manipulators," in *Proc. IEEE Int. Conf. Robot. Autom.*, Saint Paul, MN, USA, 2012, pp. 5392–5397.
- [32] R. E. Goldman, A. Bajo, and N. Simaan, "Compliant motion control for continuum robots with intrinsic actuation sensing," in *Proc. IEEE Int. Conf. Robot. Autom.*, Shanghai, China, 2011, pp. 1126–1132.
- [33] H. Wang, W. Chen, X. Yu, T. Deng, X. Wang, and R. Pfeifer, "Visual servo control of cable-driven soft robotic manipulator," in *Proc. IEEE/RSJ Int. Conf. Intell. Robots Syst.*, Tokyo, Japan, 2013, pp. 57–62.
- [34] T. Mahl, A. Hildebrandt, and O. Sawodny, "A variable curvature continuum kinematics for kinematic control of the bionic handling assistant," *IEEE Trans. Robot.*, vol. 30, no. 4, pp. 935–949, Aug. 2014.
- [35] P. Merriaux, Y. Dupuis, R. Bouteau, P. Vasseur, and X. Savatier, "A study of Vicon system positioning performance," *Sensors*, vol. 17, no. 7, p. 1591, 2017.
- [36] C. Forster, L. Carbone, F. Dellaert, and D. Scaramuzza, "On-manifold preintegration for real-time visual-inertial odometry," *IEEE Trans. Robot.*, vol. 33, no. 1, pp. 1–21, Feb. 2017.
- [37] B. A. Jones and I. D. Walker, "Kinematics for multisection continuum robots," *IEEE Trans. Robot.*, vol. 22, no. 1, pp. 43–55, Feb. 2006.
- [38] J. Lai, K. Huang, B. Lu, Q. Zhao, and H. K. Chu, "Verticalized-tip trajectory tracking of a 3D-printable soft continuum robot: Enabling surgical blood suction automation," *IEEE/ASME Trans. Mechatronics*, vol. 27, no. 3, pp. 1545–1556, Jun. 2022.
- [39] R. Peng and P. Lu, "Fast adaptive complementary filter for quadrotor attitude estimation during aggressive maneuvers," in *Proc. Int. Conf. Unmanned Aircr. Syst. (ICUAS)*, 2021, pp. 182–187.
- [40] G. Zhang et al., "Grasp a moving target from the air: System & control of an aerial manipulator," in *Proc. IEEE Int. Conf. Robot. Autom.*, Brisbane, QLD, Australia, 2018, pp. 1681–1687.



Rui Peng received the B.Eng. degree in measurement and control engineering and the M.Sc. degree in electronics communication from Wuhan University, Wuhan, China, in 2018 and 2020, respectively. He is currently pursuing the Ph.D. degree in mechanical engineering with the Adaptive Robotics Lab, The University of Hong Kong, Hong Kong.

His research interests involve aerial manipulation, vision-based robotic control, and motion planning.



Peng Lu received the bachelor's and master's degrees in flight control from Northwestern Polytechnical University, Xi'an, China, in 2010 and 2013, respectively, and the Ph.D. degree in flight control from the Delft University of Technology, Delft, The Netherlands, in 2016.

He is currently an Assistant Professor with the Department of Mechanical Engineering, The University of Hong Kong (HKU), Hong Kong. Before he joined HKU in 2020, he was an Assistant Professor with The Hong Kong Polytechnic University, Hong Kong, and a Postdoctoral Researcher with ETH Zürich, Zürich, Switzerland. His research interests involve nonlinear adaptive control for aircraft, including UAVs, trajectory planning, reinforcement learning, and vision-based navigation and control.



Zehao Wang received the B.Eng. degree in mechanical engineering from Jilin University, Jilin, China, in 2018, and the M.Sc. degree in mechanical engineering from The University of Hong Kong, Hong Kong, in 2021.

During the Postgraduate studies, he worked in mechanical engineering with the Adaptive Robotics Lab, The University of Hong Kong. His research interests involve lightweight design of aerial manipulators.